ELSEVIER

Journal of Power Sources 102 (2001) 82–96

JOURNAL OF POWER SOURCES

www.elsevier.com/locate/jpowsour

Mathematical modeling of proton exchange membrane fuel cells

Andrew Rowe[a], Xianguo Li[b,*]

[a]Department of Mechanical Engineering, University of Victoria, Victoria, BC, Canada
[b]Department of Mechanical Engineering, University of Waterloo, Waterloo, Ont., Canada

Received 11 September 2000; received in revised form 20 March 2001; accepted 27 March 2001

Abstract

A one-dimensional non-isothermal model of a proton exchange membrane (PEM) fuel cell has been developed to investigate the effect of various design and operating conditions on the cell performance, thermal response and water management, and to understand the underlying mechanism. The model includes variable membrane hydration, ternary gas mixtures for both reactant streams, phase change of water in the electrodes with unsaturated reactant gas streams, and the energy equation for the temperature distribution across the cell. It is found that temperature distribution within the PEM fuel cell is affected by water phase change in the electrodes, especially for unsaturated reactant streams. Larger peak temperatures occur within the cell at lower cell operating temperatures and for partially humidifed reactants as a result of increased membrane resistance arising from reduced membrane hydration. The non-uniform temperature rise can be significant for fuel cell stacks. Operation on reformed fuels results in a decrease in cell performance largely due to reduced membrane hydration, which is also responsible for reduced performance at high current densities for high cell operating pressures. Model predictions compare well with known experimental results.

Keywords: Proton exchange membrane (PEM); Electrodes; Catalyst layers; Fuel cells; Modelling

1. Introduction

There is an increasing interest in the use of proton exchange membrane (PEM) fuel cells for both mobile and stationary applications as an environmentally friendly power source. Emphasis is placed on high power density with adequate energy conversion efficiency for mobile applications, and on high energy efficiency with adequate power density for stationary applications. Two key issues limiting the widespread commercialization of fuel cell technology are better performance and lower cost. PEM fuel cell performance is limited by polarizations. A good understanding of the effect of design and operating conditions on the cell potential is required in order to reduce polarization. Major operating parameters include cell temperature, pressure, reactant stoichiometry, and gas stream composition. Cell structure and materials are also of importance. Some problems particular to PEM fuel cells result from the use of an ionomer as electrolyte. For example, the solubility of a reactant gas in, and the ionic resistivity of, the electrolyte depend on the membrane moisture content and temperature. As a result, the membranes require adequate humidification for proper performance. Humidification is often achieved via water vapor in the reactant gas streams; however, excessive water presence, especially water production at high power density from cell reactions, can lead to the flooding of the electrode pores, thereby limiting gas-transport to the reaction sites. Increasing the operating temperature can decrease mass-transport limitations and increase the electrochemical reaction rates; but increased temperature also has an adverse effect on the maximum cell potential due to thermodynamic considerations and the increase in water vapor partial pressure. Thus, both thermal and water management are critical to the performance of PEM fuel cells.

In the last decade a number of fundamental studies have been directed towards increasing our understanding of PEM fuel cells and their performance. One of the earlier studies by Bernardi [1] focused on the humidification requirements of inlet gases in order to mainatain water balance in a PEM cell. Bernardi and coworkers continued to investigate the performance of a gas-fed porous cathode bonded to an ion-exchange membrane [2], and developed a one-dimensional isothermal cell model [3]. On the other hand, Wang and Savinell [4] studied the hydrogen electrode bonded to a membrane, and examined the effect of carbon monoxide poisoning of the platinum catalyst. Humidified hydrogen is the anode gas. Springer and his colleagues have made significant contributions to the understanding of the processes occurring in a PEM fuel cell. An early study developed an isothermal, one-dimensional, steady-state model of

* Corresponding author. Tel.: +1-519-888-4567; fax: +1-519-888-6197.

0378-7753/01/$ – see front matter
PII: S0378-7753(01)00798-4

a complete PEM fuel cell [5], including variable membrane hydration. The anode catalyst layer was neglected and the cathode catalyst layer was taken to be a thin reactive plane.

Fuller and Newman [6] investigated the water and thermal management in PEM fuel cells, and Nguyen and White studied the effects of various forms of gas humidification on cell performance and water management [7]. Further work by Wilson et al. fit a number of cell performance curves using experimentally determined parameters [8]. This model included interfacial kinetics at the Pt/ionomer interface, gas-transport and ionic-conductivity limitations in the catalyst layer, and gas-transport limitations in the cathode backing. From the comparison of their model predictions with the experimental data, they concluded that the permeability of reactant gas in their thin-film catalyst structures was approximately three orders of magnitude higher than in neat ionomer. Yong et al. [9] conducted both experimental and modeling studies, and found that with an oxygen mole fraction greater than 0.4 (dry gas), mass transport effects were considerably reduced; very low diffusion coefficients of oxygen in the substrate layer were necessary to explain the rapid reduction in cell potential at high current densities.

Amphlett et al. [10,11] developed a parametric model of a single PEM cell by using a mechanistic approach, and a number of grouped parameters were identified and fit to the empirical data measured from a Ballard Mark IV single cell. Similarly, Kim et al. used an empirical equation to describe the performance data of a PEM fuel cell over the complete operating range [12]. The inclusion of an exponential term with an adjustable parametric coefficient was found to accurately model the performance curves up to and including the mass transport limited region at high current densities.

Grot et al. [13] modelled an isothermal, steady, one-dimensional PEM cell incorporating the membrane water model from [5]. For the catalyst layer, it was assumed that the catalyst particles were covered by a thin film of ionomer and that diffusion through this film could be neglected. Marr and Li [14] extended Grot et al.'s model, and investigated the catalyst utilization as well as the optimal composition and structure for the cathode catalyst layer, such as the catalyst loading, catalyst type (e.g. platinum black or supported on carbon), catalyst layer thickness, void fraction, and ionomer content. Most of these modeling results agreed surprisingly well with the experimental data obtained in an indenpendent study by a team of Ballard researchers [15]. Marr and Li [16] further developed a cell model with engineering correlations for transport phenomena in the reactant flow channels. A recent study by Baschuk and Li [17] included the variable degree of liquid water flooding in the catalyst layer and electrode backing regions as well as their effect on the cell performance. Baschuk and Li [18] also examined the issue of carbon monoxide poisoning in PEM fuel cells. A recent model by Wohr and Bolwin [19] has particular relevance to the present study as their results described the temperature profile across a number of PEM cells.

Clearly most of the previous studies either deal with the cell performance or water and thermal issues separately, even though they are closely related and cell performance is significantly influenced by the water and thermal management. Therefore, the objective of the present study is to develop a detailed cell performance and thermal model incorporating water and temperature distribution in the cell, and to investigate the operating conditions on the cell performance as well as temperature and water distribution. Such a study will be useful for the design and operation of practical fuel cells and stacks where appropriate cell cooling system affects output power density and contributes significantly to the cost of PEM fuel cells.

2. Model formulation

Consider a typical PEM fuel cell, as shown in Fig. 1. It consists of a cathode and anode electrode with a proton-conducting membrane as the electrolyte sandwiched in between. Between each of the electrodes and the membrane there exists a catalyst layer, referred to as the cathode and anode catalyst layer, respectively. Therefore, a total of five distinct regions need to be modelled, and the typical thickness for each region is also shown in Fig. 1.

It is assumed that the cell is steady and all the parameters change in the x-direction only, as shown in Fig. 1. This one-dimensional approach is reasonable as a first approximation considering the fact that the other dimensions of the cell are typically orders of magnitude larger than the cell thickness. The reactant gas mixtures are approximated as ideal gases, and reactant cross-over and electrode corrosion are insignificant at practical operating conditions with negligible viscous, Soret, Dufour, gravity and radiation effects as well as negligible pressure changes in an electrode. Thermophysical properties are evaluated at the average cell temperature because of small temperature variations across the cell as shown later in this study. The cathode catalyst layer is regarded to be fully hydrated as product water is produced there and the reactant streams are usually fully humidified. This assumption is reasonable as Baschuk and Li [18] indicated. The anode catalyst layer hydration is taken as a function of water vapor activity, similar to Springer and coworkers [8,20]. The catalyst is uniformly distributed in both the cathode and anode catalyst layers, and the dissolution of reactant gases in liquid water follows Henry's law. Also for simplicity, a linear variation across the electrolyte membrane is assumed for both the hydration of the electrolyte membrane and the pressure difference between the anode and the cathode. With these assumptions the cell model is formulated with transport phenomena for the electrodes, catalyst layers and membrane electrolyte as described in the following sections. Details of the model formulation, derivations of the governing equations, solution method and numerical procedures can be found in [21].

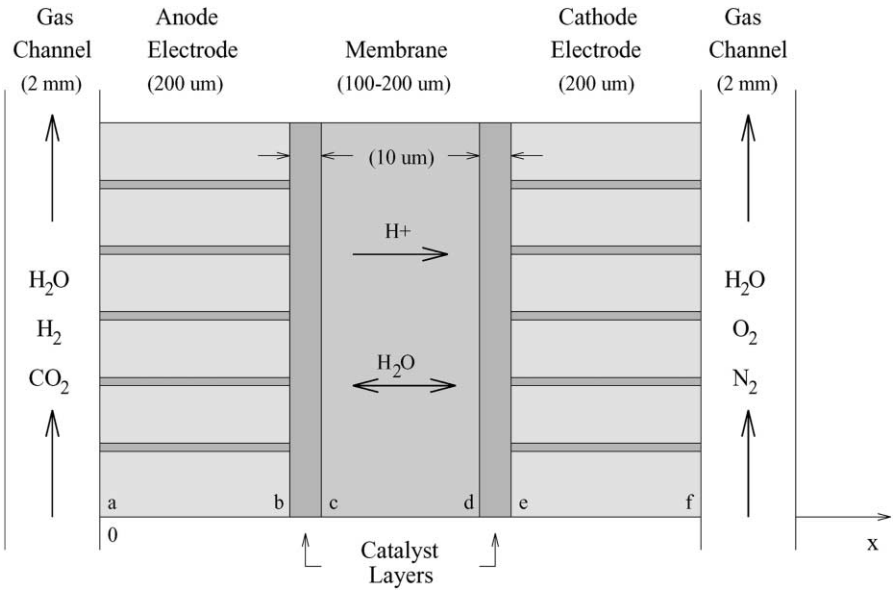

Fig. 1. A schematic of a PEM fuel cell.

2.1. Electrodes

The electrode, as defined here, consists of a gas-transport substrate only which serves the purposes of current collection and gas-transport to reaction sites. The electrode corresponds to regions a–b and e–f shown in Fig. 1.

The mathematical model of the various transport processes occurring in the electrode is formulated by applying the conservation equations for an ideal gas in a porous media. Specifically, the conservation of species and energy are applied along with the Stefan–Maxwell equation for multi-component gas diffusion and Fourier's law for heat conduction. It is assumed that there is negligible pressure gradient and the primary means of gas-transport is diffusion. The governing equations are

$$\text{species}: \quad \nabla \cdot (\rho_i \vec{v} + \rho_i \vec{V}_i) = w_i \tag{1}$$

$$\text{energy}: \quad \rho \vec{v} \cdot \nabla u = -\nabla \cdot \vec{q} - p \nabla \cdot \vec{v} + \dot{q}_s \tag{2}$$

$$\text{where} \quad \vec{q} = -k^{\text{eff}} \nabla T + \rho \sum_i h_i Y_i \vec{V}_i \tag{3}$$

where ρ_i is the partial density of species i, $\vec{v}$ the mass-averaged velocity and $\vec{V}_i$ the species diffusion velocity, u the internal energy, $\vec{q}$ the diffusive heat flux, k^{eff} the effective thermal conductivity, h_i the specific enthalpy, p the pressure, T the temperature and Y_i the mass fraction of species i. The mass and energy source w_i and $\dot{q}_s$ account for the addition of mass and energy to the gas mixture due to the vaporization of liquid water and Joule heating due to electrical current flow, respectively.

The sum of the individual species equations gives the overall continuity equation for the gas mixture

$$\text{continuity}: \quad \nabla \cdot (\rho \vec{v}) = \sum_i w_i \tag{4}$$

and the diffusion velocity, $\vec{V}_i$, can be determined from the Stefan–Maxwell equation for multi-component gas diffusion

$$\nabla x_i = \sum_j \left(\frac{x_i x_j}{D_{ij}^{\text{eff}}} \right) (\vec{V}_j - \vec{V}_i) \tag{5}$$

where D_{ij}^{eff} is the effective binary diffusion coefficient for species i in j, and x_i is the mole fraction for species i. The binary diffusion coefficients are calculated with the emperical correlation of Fuller, Schettler, and Giddings as found in [34].

The oxidant used in terrestrial applications of PEM fuel cells is almost invariably humidified air. Hence, the species i are defined as $1 = O_2$, $2 = N_2$, $3 = H_2O$ (g) (here the symbol "g" represents water vapor) for the cathodic electrode; and $1 = H_2$, $2 = CO_2$, and $3 = H_2O$ (g) for anodic electrode. Such a designation takes into account the possibility of using both pure hydrogen and hydrocarbon reformed gases as fuel. It should be noted that for a reaction rate set by cell current density I, the mole flux of hydrogen is twice that of oxygen due to stoichiometric requirement, which is denoted by the parameter n. Hence, n represents the moles of electrons transferred per mole of reactant (H_2 or O_2) consumed.

The above governing equations can be simplified for the present one-dimensional transport processes as follows:

$$\text{species 1}: \quad \frac{dx_1}{dx} = \frac{RT}{p} \left[\frac{x_1 N_3 - x_3 N_1}{D_{13}^{\text{eff}}} - \frac{x_2 N_1}{D_{12}^{\text{eff}}} \right] \tag{6}$$

$$\text{pecies 3}: \quad \frac{dx_3}{dx} = \frac{RT}{p} \left[\frac{x_3 N_1 - x_1 N_3}{D_{13}^{\text{eff}}} - \frac{x_2 N_3}{D_{23}^{\text{eff}}} \right] \tag{7}$$

$$\text{species 2}: \quad x_2 = 1 - x_1 - x_3 \tag{8}$$

$$\text{energy}: \quad -k^{\text{eff}}\frac{\mathrm{d}^2T}{\mathrm{d}x^2} + \left[\left(\frac{I}{nF}\right)W_1c_{p,1} + N_3W_3c_{p,3} + N_\ell W_3c_{p,\ell}\right]\frac{\mathrm{d}T}{\mathrm{d}x} + h_{\text{vap}}w_3 - \frac{I^2}{\sigma^{\text{eff}}} = 0 \tag{9}$$

$$\text{flux}: \quad \frac{\mathrm{d}}{\mathrm{d}x}(N_3) = \frac{w_3}{W_3} \tag{10}$$

$$\text{source}: \quad w_3 = Sh\frac{D_3^{\text{eff}}}{L}f_{\text{e}}\frac{pW_3}{RT}\left(\frac{p_{\text{sat}}}{p} - x_3\right) \tag{11}$$

$$\text{potential}: \quad \frac{\mathrm{d}\Phi_{\text{s}}}{\mathrm{d}x} = -\frac{I}{\sigma^{\text{eff}}} \tag{12}$$

where the subscript "ℓ" denotes liquid water, R is the universal gas constant, N the molar flux, F the Faraday constant, W the molecular weight, c_p the specific heat at constant pressure, h_{vap} the enthalpy of vaporization for water, σ^{eff} the effective electrical conductivity, D_3^{eff} the effective diffusion coefficient for water vapor in the gas mixture, p_{sat} the saturation pressure of water, and Φ_{s} the electrical potential in the solid matrix of the electrode. The mass source, w_3, which is the rate of water vaporization or condensation, depends on the Sherwood number, Sh, surface area of liquid water per unit volume, f_{e}, and the characteristic length scale L involved. Eq. (12) is just the Ohm's law. Clearly, for each of the electrode regions there are seven equations for seven unknowns: $x_1, x_2, x_3, T, N_3, w_3$ and Φ_{s}.

2.2. Catalyst layers

Although the catalyst layers are relatively small, they are the heart of the fuel cell. Here fuel and oxidant react electrochemically to produce electrical energy. In this region of the cell, the transfer of mass and energy is coupled with reaction kinetics and results in a potential difference between electrodes. How this potential difference varies as a function of mass transfer, electrode kinetics, and energy flux determines the cell performance.

In this study the catalyst layers are assumed to be a mixture of membrane, catalyst and void space. The volume fractions of these components can be varied as can the effective surface area of catalyst that is characterized by different loadings and catalyst types. The overall reactions in the cathode and anode catalyst layers are taken as

$$\text{cathode}: \quad \mathrm{O_2(aq)} + 4\mathrm{H^+(aq)} + 4\mathrm{e^-(Pt)} \rightarrow 2\mathrm{H_2O}(\ell) \tag{13}$$

$$\text{anode}: \quad \mathrm{H_2(aq)} \rightarrow 2\mathrm{H^+} + 2\mathrm{e^-} \tag{14}$$

Using the subscript notation of $1 = \mathrm{O_2}$, $2 = \mathrm{H^+}$, and $3 = \mathrm{H_2O}(\ell)$ for the cathode catalyst layer, and $1 = \mathrm{H_2}$, $2 = \mathrm{H^+}$, and $3 = \mathrm{H_2O}(\ell)$ for the anode catalyst layer, respectively, a set of governing equations can be derived, similar to the electrode regions described earlier, by an application of the conservation laws for the species and energy along with the Butler–Volmer equation for the electrochemical reactions, the Nernst–Planck equation for the flux of aqueous species in the membrane, electroneutrality, and Fourier's law for heat conduction. The energy equation includes heat production due to both reversible and irreversible mechanisms. Species diffusion and Ohm's law for electron transfer in the solid matrix complete the formulation, which is

$$\text{flux 1}: \quad \frac{\mathrm{d}N_1}{\mathrm{d}x} = \frac{-\nu_1 j(x)}{nF} \tag{15}$$

$$\text{flux 2}: \quad \frac{\mathrm{d}i_{\text{m}}}{\mathrm{d}x} = j(x) \tag{16}$$

$$\text{flux 3}: \quad \frac{\mathrm{d}N_3}{\mathrm{d}x} = \frac{-\nu_3 j(x)}{nF} \tag{17}$$

$$\text{energy}: \quad -k^{\text{eff}}\frac{\mathrm{d}^2T}{\mathrm{d}x^2} + \left(N_1c_{p,1}W_1 + N_3c_{p,3}W_3\right)\frac{\mathrm{d}T}{\mathrm{d}x} + \left|\frac{j(x)}{nF}\right|(T\,\Delta\bar{s}) = j(x)(\Phi_{\text{s}} - \Phi_{\text{m}}) + \frac{i_{\text{m}}^2}{\kappa^{\text{eff}}} \tag{18}$$

$$c_1: \quad D_1^{\text{eff}}\frac{\mathrm{d}^2c_1}{\mathrm{d}x^2} - \frac{N_3}{c_3}\frac{\mathrm{d}c_1}{\mathrm{d}x} - \frac{c_1}{c_3}\frac{\mathrm{d}N_3}{\mathrm{d}x} + \frac{\mathrm{d}N_1}{\mathrm{d}x} = 0 \tag{19}$$

$$\Phi_{\text{m}}: \quad \frac{\mathrm{d}\Phi_{\text{m}}}{\mathrm{d}x} = -\frac{i_{\text{m}}}{\kappa^{\text{eff}}} + \frac{F}{\kappa^{\text{eff}}}\frac{c_2}{c_3}N_3 \tag{20}$$

$$\Phi_{\text{s}}: \quad i_{\text{s}} = -\sigma^{\text{eff}}\frac{\mathrm{d}\Phi_{\text{s}}}{\mathrm{d}x} \tag{21}$$

where

$$j(x) = ai_0^{\text{ref}}\left(\frac{c_1}{c_1^{\text{ref}}}\right)^{\gamma_1}\left[\exp\left(\frac{\alpha_{\text{a}}F}{RT}(\Phi_{\text{s}} - \Phi_{\text{m}})\right) - \exp\left(-\frac{\alpha_{\text{c}}F}{RT}(\Phi_{\text{s}} - \Phi_{\text{m}})\right)\right] \tag{22}$$

the Butler–Volmer equation, here ν_i the stoichiometric coefficient for species i in the cathodic and anodic reactions as given in Eqs. (13) and (14), $\Delta\bar{s}$ the entropy change for these two reactions, Φ the electrical potential, D the diffusion coefficient, c the concentration, κ the electrical conductivity of the membrane, i_{m} and i_{s} are the current density in the proton-conducting membrane and the electron-conducting solid, respectively, i_0^{ref} the reference exchange current density at the reference concentration c_1^{ref}, and a the catalyst reactive surface area per unit volume. Because no water is produced by the anodic reaction, Eq. (14), $\nu_3 = 0$ for the anode catalyst layer. The transfer coefficient α_a and α_{c} in the Butler–Volmer equation are taken as unity. This gives an approximate Tafel slope of 70 mV/decade, which is similar to that used by Springer, et al. [20]. Hence, for each of the catalyst layers, there are seven equations for seven unknowns: N_1, i_{m}, N_3, T, c_1, Φ_{m} and Φ_{s}.

2.3. Membrane electrolyte

For PEM fuel cells, a perfluorosulfonate polymer membrane acts as the hydrogen ion conductor. The transport processes in the membrane are described by the conservation of species and energy. The net flux of water across the membrane is determined by the net effect of electro-osmotic drag, diffusion due to concentration gradient, and convection due to a pressure gradient. The flux of protons is described by the Nernst–Planck equation. Hence, the governing equations are

$$\text{energy}: \quad -k^{\text{eff}}\frac{\mathrm{d}^2T}{\mathrm{d}x^2}+\frac{\mathrm{d}}{\mathrm{d}x}(N_\ell h_\ell W_\ell)=\frac{i_{\text{m}}^2}{\kappa} \tag{23}$$

$$\text{potential}: \quad \frac{\mathrm{d}\Phi_{\text{m}}}{\mathrm{d}x}=-\frac{i_{\text{m}}}{\kappa}+\delta\frac{RT}{F}\left(\frac{3}{1+\delta\lambda}\right)\frac{\mathrm{d}\lambda}{\mathrm{d}x}+\frac{F}{\kappa}\left(\frac{1}{\lambda}\right)N_\ell \tag{24}$$

$$\text{hydration}: \quad \lambda=\lambda_{\text{a}}+\left(\frac{\mathrm{d}\lambda}{\mathrm{d}x}\right)(x-t_{\text{c}}) \tag{25}$$

$$\text{Water Flux}: \quad N_\ell=-D_\ell\left(\frac{\mathrm{c}_{\ell,\text{c}}-c_{\ell,\text{a}}}{t_{\text{m}}}\right)-\epsilon_{\text{w}}^{\text{mem}}c_\ell\frac{k_{\text{P}}}{\mu}\left(\frac{p_{\text{c}}-p_{\text{a}}}{t_{\text{m}}}\right)+\frac{\eta_{\text{d}}I}{F} \tag{26}$$

where the subscript "a" and"c" are for quantities at the anode and cathode side of the membrane; δ is the membrane expansion coefficient with hydration; k_{P} and μ are the hydraulic permeability of the membrane and liquid water viscosity, respectively; t_{m} the thickness of the membrane, $\epsilon_{\text{w}}^{\text{mem}}$ the volume fraction of water in the membrane, and η_{d} the electro-osmotic drag coefficient. Zawodzinski et al. [5] determined δ to be 0.0126 for Nafion 117; it is assumed that this value applies to all membranes and is independent of temperature and pressure. In the above equations, the membrane hydration λ, concentration and pressure have been assumed to vary linearly. These are deemed to be suitable first assumptions. Although a linear variation in hydration does not imply a corresponding variation for water concentration, this approximation has been employed for numerical simplicity.

The hydration at the anode side of the membrane is determined by the activity of water vapor, a, there. An empirical correlation based on the adsorption isotherm of Nafion 117 is used with an allowance for the activity to exceed unity. A maximum hydration of 16.8 is assumed in the presence of liquid water as measured by Zawodzinski for Nafion 117 immersed in water at 80°C [5]. The hydration is assumed to vary linearly from 14 to 16.8 when the mole fraction of water vapor exceeds saturation up to $3x_{\text{sat}}$ in a manner similar to that used in [5, 30].

$$\lambda=0.043+17.81a-39.85a^2+36.0a^3,\quad 0<a=\frac{x_3p}{p_{\text{sat}}}\le 1 \tag{27}$$

$$\lambda=14+1.4\left(\frac{x_3p}{p_{\text{sat}}}-1\right),\quad 1<a=\frac{x_3p}{p_{\text{sat}}}\le 3 \tag{28}$$

The osmotic drag is quantified by η_{d}, the electro-osmotic drag coefficient which is defined as the ratio of moles of water transported per mole of protons where there is no concentration or pressure gradient. Zawodzinski et al. have measured drag coefficients as high as 4.0 in fully hydrated samples of membrane C, while Nafion 117 exhibited $\eta_{\text{d}}=2.5$ for $\lambda=22$, and $\eta_{\text{d}}=0.9$ for $\lambda=11$ [32]. For this work, the osmostic drag coefficient is assumed to be a linear function of hydration [5] with a maximum value of 1.0 for full hydration ($\lambda=16.8$). Similarly, the diffusion coefficient of water in the membrane D_ℓ, the membrane expansion coefficient δ and the membrane hydraulic permeability k_{P} are taken from [5].

Both the membrane proton conductivity and the diffusion coefficient for liquid water in the membrane are determined as a function of membrane hydration and temperature T (in K) [5].

$$\kappa=\exp\left[1268\left(\frac{1}{303}-\frac{1}{T}\right)\right]\times(0.005139\lambda-0.00326)\quad(\Omega\,\text{cm})^{-1} \tag{29}$$

$$D_3=1\times10^{-6}\exp\left[2416\left(\frac{1}{303}-\frac{1}{T}\right)\right]\times(2.563-0.33\lambda+0.0264\lambda^2-0.000671\lambda^3)\times(\text{cm}^2/\text{s}) \tag{30}$$

The diffusion coefficient for oxygen is determined by a similar function [29]:

$$D_{\text{O}_2}=2.88\times10^{-6}\exp\left[2933\left(\frac{1}{313}-\frac{1}{T}\right)\right]\quad(\text{cm}^2/\text{s}) \tag{31}$$

And, the diffusion coefficient for hydrogen is determined by [3]

$$D_{\text{H}_2}=4.1\times10^{-3}\exp\left[-2602\left(\frac{1}{T}\right)\right]\quad(\text{cm}^2/\text{s}) \tag{32}$$

Finally, it should be mentioned that liquid water flux was only determined explicity in the membrane region. Liquid water flux in the other regions of the cell are calculated based upon mass conservation, assuming steady-state and known flooding.

2.4. Boundary conditions

Before the governing equations formulated earlier can be solved uniquely, appropriate boundary conditions must be specified. The temperature, pressure, relative humidity, flow rate in terms of stoichiometry and composition of the reactant gas in both anode and cathode flow channels (i.e. at the point a and f shown in Fig. 1) are specified according to the cell operating conditions. Because the gas composition

changes along the flow channels due to cell reactions, the mole fractions of gas species at the boundaries a and f are determined based upon the set stoichiometric flow rate of gas and the humidification of the streams. The average composition between inlet and outlet is determined using an integral material balance on the gas chambers in a similar manner to [2]. For example, the effective mole fraction of species 1 is determined by taking the average of the inlet and outlet conditions as follows:

$$x_1 = \frac{1 - x_3}{1 + (x_{21}/2)(1 + \zeta/(\zeta - 1))} \tag{33}$$

where x_{21} is the molar ratio of species 2 to 1 in the dry gas, and ζ the stoichiometric flow rate. The electrical potential in the membrane at the interface b is set to 0 for convenience.

By assuming that liquid water and water vapor are in local thermodynamic equilibrium, the water vapor flux, N_3, could be calculated iteratively. However, due to difficulty in determining the liquid water motion through the porous electrodes, for convenience N_3 at the electrode/catalyst layer interface is set to 0.1 at b, and -0.1 at e, when normalized by the reactant gas flux at b and e, respectively, although the flux of water vapor at these boundaries will, in general, vary with operating conditions.

3. Model validation

The governing equations were non-dimensionalized and solved using an algorithm developed by Fan and White [22]. The thermophysical properties, kinetic data and details of the numerical procedures are available elsewhere [2]. It is worth emphasizing that different values have been used for the gas diffusion coefficient in the catalyst layer (aqueous phase) and in the electrode (gaseous phase); and for the proton conductivity of Nafion 117 in the catalyst layer and in the membrane, as previously described.

The present model predictions are compared to experimentally determined cell performance data for model validation. Derouin, et al. [23] and Beery, et al. [24] have explored experimentally the effects of varying catalyst loading and catalyst type. The experimental results of these works are well documented, and therefore, selected for comparison. The membrane material is assumed to have the properties of Nafion 117. Typical results are presented below.

Using the parameter values listed in Table 1, the predicted polarization curve is compared to the experimental data [23] in Fig. 2 for 20 wt.% Pt/C catalyst and air or pure oxygen at 5 atm as oxidant. It is seen that the present model predictions agree well with the experimental results for both cases. It might be pointed out that no adjustment to the reactive surface area, a, or the exchange current density, i_0^{ref}, is required to achieve the good agreement between the present model predictions and the experimental data shown in Fig. 2. The roughness factor employed (i.e. the surface area of catalyst per unit area of cell) is the average of the two values reported for 20 wt.% Pt/C catalyst, determined by cyclic voltammetry and transmission electron microscopy [24]. The electrode thickness used is lower than many values used in other modeling studies; a value of 260–300 μm is often used, which corresponds to the width of electrode material as received. Springer et al. have reported a compressed value for E-Tek electrodes of approximately 180 μm [20]; while prototech electrodes were used in [23,24]. It is

Table 1
Parameters used for the model validation

Cell temperature, T_c (K)	353.0
Anode pressure, p (atm)	3.0
Cathode pressure, p (atm)	5.0
Anode stoichiometry, ζ	1.5
Cathode stoichiometry, ζ	3.0
Anode relative humidity (%)	100
Cathode relative humidity (%)	100
Electrode thickness, t_e (μm)	180
Catalyst layer thickness, t_{cl} (μm)	10
Membrane thickness, t_m (μm)	180
Volume fraction of membrane in catalyst layer, ϵ_m^{cl}	0.17
Volume fraction of solid in catalyst layer, ϵ_s^{cl}	0.4
Catalyst layer flooding (%)	98
Anode dry gas mole fraction (CO_2/H_2) (pure H_2)	0.0
Cathode dry gas mole fraction (N_2/O_2) (air)	3.76
Reversible potential, $V_{oc}(V)$	1.21
Reactive area per unit volume, a (cm^2/cm^3)	68×10^3
Anode catalyst layer H_2 permeability, $D_1^{\mathrm{eff}} c_1^{\mathrm{ref}}$ (mol/cm s)	2×10^{-8}
Cathode catalyst layer O_2 permeability, $D_1^{\mathrm{eff}} c_1^{\mathrm{ref}}$ (mol/cm s)	7×10^{-10}
Anode: ai_0^{ref} (A/cm^3)	4000
Cathode: ai_0^{ref} (A/cm^3)	0.0013
$(Sh \times f_e)/L$ (cm^{-2})	20000

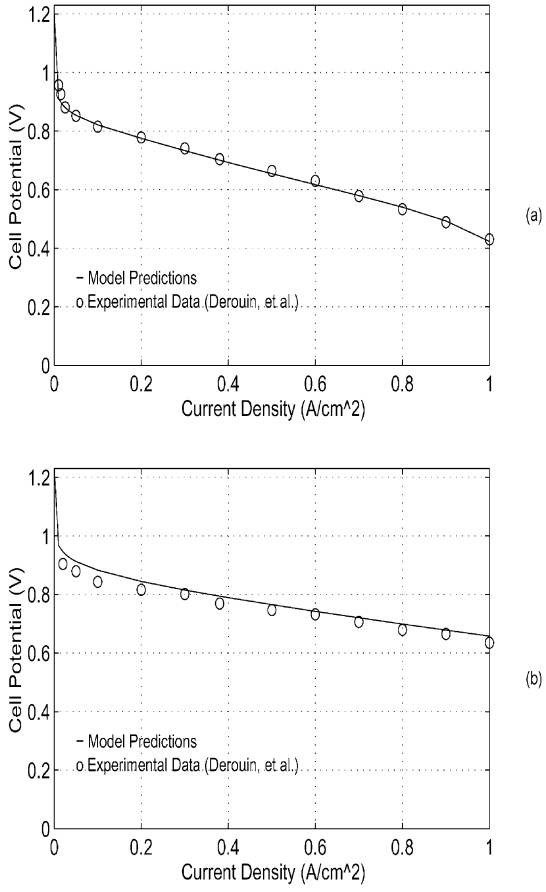

Fig. 2. Comparison between the model predictions and experimental results of Derouin et al. [23] for 20 wt.% Pt/C catalyst and air (a) or O_2 (b) at 5 atm using validation parameters in Table 1.

assumed here that these two types of electrodes have similar thickness after compression in the experiments.

The composition of the catalyst layer requires some justification. The values for the volume fraction of membrane and solid are similar to those used by Grot et al. [13] but are significantly different from those of Bernardi et al. [2,3]. The permeability of the catalyst layer has a significant impact on catalyst utilization and overall cell polarization. Work at Los Alamos National Laboratory provides evidence suggesting that permeabilites in the catalyst layer are much higher than the reported values for oxygen and hydrogen in neat ionomer [8,20]. Moreover, the work of Derouin et al. [23] suggests catalyst layer permeabilities that are higher than those used by Bernardi [3].

The effective transport parameters for thermal conductivity, electrical conductivity and mass diffusion in each of the layers are approximated by using the sum of the volume weighted parameters for each component that makes up the layer (except for the mass diffusion coefficients in the electrodes; these are discussed in [21]). In the case of the effective thermal conductivity for the catalyst layer a parallel resistance analogy is used:

$$k^{\text{eff}} = \epsilon_{\text{m}} k_{\text{m}} + \epsilon_{\text{s}} k_{\text{s}} + \epsilon_{\text{w}} k_{\text{w}}, \tag{34}$$

where the conductivity is determined by the volume fractions, ϵ, of the components making up the layer: membrane, solid (catalyst) and water. The thermal conductivity of the solid electrodes is assumed to be approximately 0.026 W/cm K.

The bulk diffusion coefficient for oxygen in the cathode catalyst layer is determined by the volume fractions of membrane, water and void space and by using a parallel resistance analogy. A parallel analogy seems to well approximate the empirical permeabilities reported for Nafion impregnated, hot-pressed, layer structures [33]:

$$D_1 = \epsilon_{\text{m}} D_1^{\text{mem}} + \epsilon_{\text{w}} D_1^{\text{w}} + \epsilon_{\text{void}} D_{ij} \tag{35}$$

where, D_{ij} is taken as the diffusion coefficient of oxygen in nitrogen for air operation and oxygen in water vapor for neat-O_2 operation. In the case of the anode, a similar approximation is made; however, for reformed fuel, D_{ij} is the diffusion coefficient of hydrogen in carbon dioxide. The effective diffusion coefficient for the catalyst layer is then determined by modifying the porosity of the layer.

$$D_1^{\text{eff}} = (1 - \epsilon_{\text{s}}) D_1 \tag{36}$$

A tortuosity correction is not employed here as there is no information available regarding the value of this parameter in a typical catalyst layer structure. The effective electrical conductivity of the membrane phase in the catalyst layers is modified for porosity in a similar manner. Coefficient values for diffusion, concentration, and conductivity are temperature dependent and are not constant throughout the MEA. Property values are calculated for each node position depending on the temperature at the particular node. The permeabilty values listed in Tables 1 and 2 are calculated values at near zero current density (10 mA/cm^2) and are shown for reference only, not as constant values.

4. Result and discussion

The PEM fuel cell model developed in the preceding sections makes it possible to explore the effect that operating conditions, physical morphology, and kinetics have on cell performance. The model base conditions given in Table 2 are derived from data available in the literature and from the physical and kinetic data given elsewhere [21]. The most significant difference between the parameter values given here and those in Table 1 for the model validation is the volume composition of the catalyst layers. These values, similar to Bernardi and Verbrugge [2,3], provide a realistic value for the thermal conductivity of the layer.

The cell polarization curve resulting from the base case parameters is shown in Fig. 3. As expected, the most significant contributor to potential loss for the cell is the cathode catalyst layer. A low permeability and exchange current density combine to demand a significant portion of the reaction free energy. The membrane layer shows a

Table 2
Base case model parameters

Cell temperature, T_c (K)	353.0
Anode pressure, p (atm)	3.0
Cathode pressure, p (atm)	3.0
Anode stoichiometry, ζ	1.5
Cathode stoichiometry, ζ	3.0
Relative humidity (%)	100
Electrode thickness, t_e (μm)	200
Catalyst layer thickness, t_{cl} (μm)	7
Membrane thickness, t_m (μm)	180
Volume fraction of membrane in catalyst layer, ϵ_m^{cl}	0.45
Volume fraction of solid in catalyst layer, ϵ_s^{cl}	0.5
Catalyst layer flooding (%)	99
Anode dry gas mole fraction (CO_2/H_2) (pure H_2)	0.0
Cathode dry gas mole fraction (N_2/O_2) (air)	3.76
Reversible potential, V_{oc} (V)	1.199
Reactive area per unit volume, a (cm^2/cm^3)	1×10^5
Anode catalyst layer H_2 permeability, $D_1^{eff} c_1^{ref}$ (mol/cm s)	8.9×10^{-10}
Cathode catalyst layer O_2 permeability, $D_1^{eff} c_1^{ref}$ (mol/cm s)	5.4×10^{-10}
Anode: ai_0^{ref} (A/cm^3)	30000
Cathode: ai_0^{ref} (A/cm^3)	0.0095
Thermal conductivity k^{eff}	
Electrodes (W/cm k)	0.016
Catalyst layers (W/cm k)	0.015
Membrane (W/cm k)	0.0034
$(Sh \times f_e)/L$ (cm^{-2})	20000

sizable potential loss due to low ionic conductivity. The loss in the anode catalyst layer is insignificant due to the relatively high permeability of H_2 and, more importantly, because the anode reaction is orders of magnitude faster than the cathode for a given activation overpotential.

The morphology and physical composition of the catalyst layer has a significant impact on cell polarization and a substantial amount of research is being conducted in hopes of optimizing the structure [23–27]. Essentially, the two main areas of focus are (1) decreasing the amount of precious metal catalyst while ensuring a large reactive surface area, and (2) increasing gas permeability in the layer for better reactant access to the reactive sites. The latter can be achieved by a number of techniques, such as wet-proofing, void space inclusion, and catalyst composition. One effective method of reducing the activation polarization for a given current density is by increasing the reactive surface area. The active surface area per unit volume, a, depends on catalyst loading, layer thickness and catalyst morphology, and ranges from 1×10^4 to 1×10^8 cm^{-1} [9,24], as found in literature. The effect of increasing a for the cathode catalyst layer from 1×10^5 to 1×10^6 cm^{-1} is shown in Fig. 4a. A decrease in the cathode activation polarization across the entire current range is evident when compared to Fig. 3.

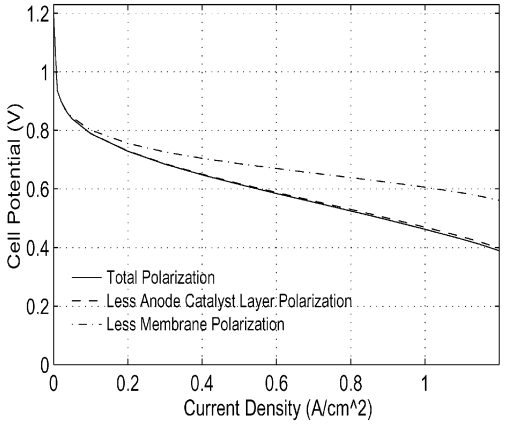

Fig. 3. Base case polarization curve using parameters in Table 2.

Fig. 4b shows the effect of increased oxygen permeability in the cathode catalyst layer on cell polarization. With low permeability, oxygen concentration is limited to a narrow region at the electrode interface [3]. In order to simulate a "high-performance" MEA, the permeability in the oxygen catalyst layer was increased by a factor of 10 as compared to the base case conditions and a high catalyst active surface area was maintained. For practical fuel cells operating at higher current densities oxygen will be confined to a thin region next to the electrode interface, and all the oxygen arriving there will be almost completely consumed by the electrochemical reactions. The polarization curve for a "high-performance" MEA at 353 K is shown in Fig. 4b and it is clear that high permeabilty catalyst layers can have a large impact on performance especially at high current densities.

Excessive low or high operating temperatures tend to affect cell performance adversely. Fig. 5 shows the predicted cell polarization curves at two different cell temperatures

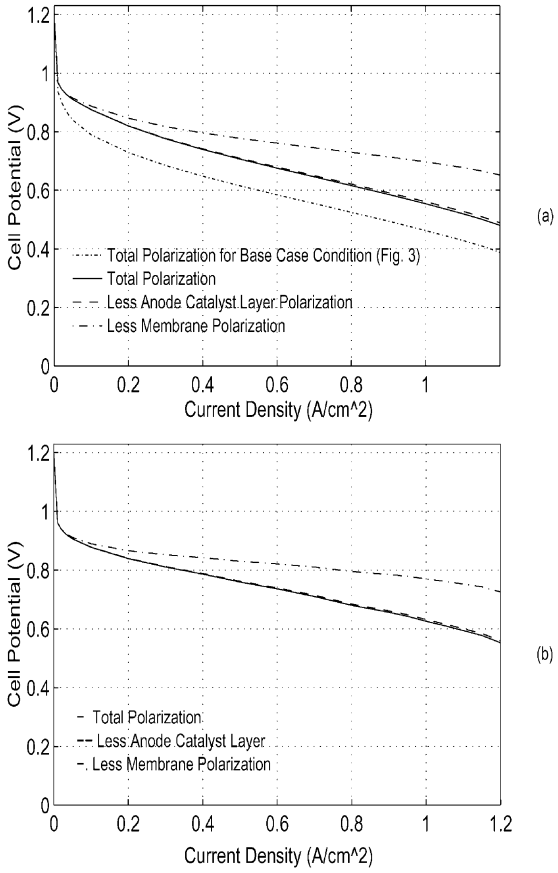

Fig. 4. (a) Cell polarization with cathode active surface area at 1×10^6 cm^2/cm^3 compared to the base case; ($a = 1 \times 10^5$ cm^2/cm^3). (b) cell potential for a "high-performance" MEA ($a = 1 \times 10^6$ cm^2/cm^3 and catalyst layer permeability = 10 × base case.)

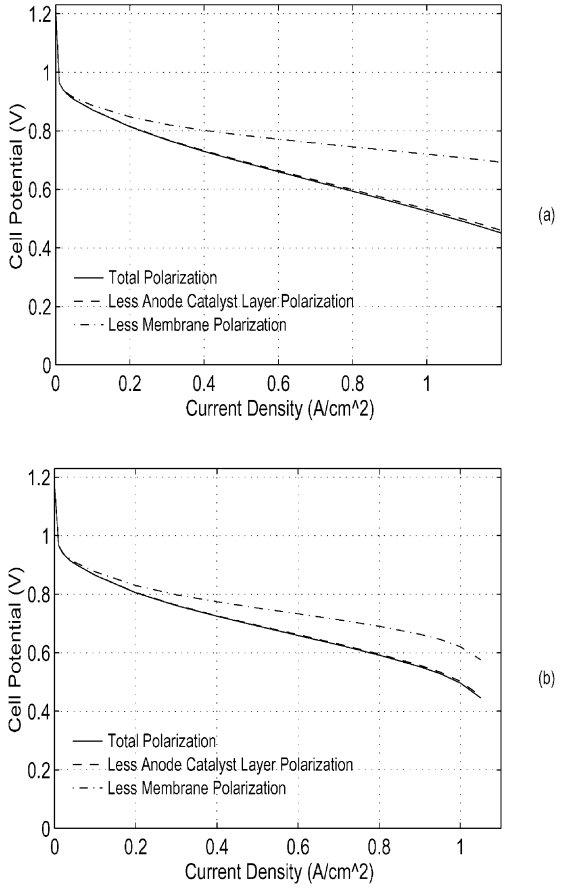

Fig. 5. Cell polarization curve for high permeability, $a = 1 \times 10^6$ cm^{-1} and $T_c = 333$ K (a); and 368 K (b) showing the effects of lower and higher operating temperature.

T_c for high permeability (10 × base case), and a cathode reactive area of 1×10^6 cm^2/cm^3 — the so-called "high-performance" MEAs. At $T_c = 333$ K (or 60°C) shown in Fig. 5a, a noticeable decrease in cell potential is evident when compared with Fig. 4b which is calculated for the same conditions except for a cell temperature of 80°C. This lower performance is primarily due to increased resistive losses in the membrane at lower cell temperatures.

Although increasing the cell operating temperature can reduce transport losses and favourably affect reaction kinetics, it can result in decreased cell potential mainly due to an increased water vapor partial pressure, leading to enhanced mass transport related losses. Fig. 5b presents the cell performance at $T_c = 368$ K (i.e. 95°C). It is seen that the cell potential is again significantly lower than that given in Fig. 4b and decreases faster for higher current densities. At approximately 1.0 A/cm^2 the concentration polarization becomes dominant due to the limitation of mass transport. The partial pressure of oxygen at the catalyst layer/cathode electrode interface becomes so small that a limiting current density is reached at about 1.1 A/cm^2. This limiting current density is estimated from the oxygen concentration distribution in the cathode electrode, as shown in Fig. 6. The horizontal coordinate is the distance within the cathode electrode normalized by the cathode electrode thickness, so that the normalized distance of "0" represents the interface between the cathode electrode and the cathode catalyst

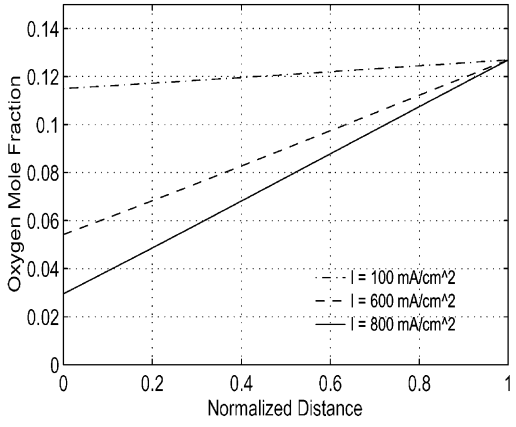

Fig. 6. Distribution of O_2 mole fraction in the cathode electrode for the same conditions as for Fig. 5b. The right-hand side ($x = 1$) is the oxidant gas channel and the left-hand side ($x = 0$) is the interface with the catalyst layer.

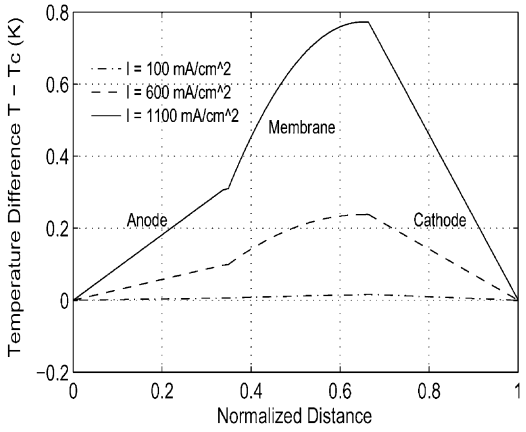

Fig. 7. Temperature distribution over the entire cell for base case conditions.

layer. It is clear that the oxygen concentration distribution within the cathode electrode, and at the electrode/catalyst layer interface, decreases as current density is increased. At the cell current density of $I = 0.8$ A/cm^2 the oxygen mole fraction at the interface reduces to about 0.03. Extrapolation indicates that the oxygen mole fraction at the interface almost vanishes at $I \approx 1.1$ A/cm^2, which is taken as the limiting current density.

The temperature profile across the entire cell is shown in Fig. 7 for the base case condition given in Table 2. It is seen that at low current density of 0.1 A/cm^2 the temperature across the cell is nearly uniform. For higher current density of 0.6 and 1.1 A/cm^2, the temperature profile is almost linear in the anode and cathode electrode, indicating heat conduction is predominant there and the heat generation due to Joule heating is not significant. However, the temperature distribution within the membrane is highly non-linear because of the significant heat generation due to Joule heating. Although the reactant gas streams are fully humidified before entering the cell, higher temperatures within the cell will result in the vaporization of liquid water, which, coupled with the electro-osmotic drag of water from the anode side to the cathode side of the membrane, will cause dehydration of the membrane on the anode side. Membrane dehydration will increase the resistance to proton migration, resulting in even more heat generation. This self-accelerating mechanism makes membrane hydration a critical parameter governing the cell performance [28]. At present, gas stream humidification is the most common means of maintaining membrane hydration [1,6,7,28], and this technique may not be adequate for high-performance PEM fuel cells which typically operate at high current densities. The non-uniform temperature distribution may become even more pronounced for fuel cell stacks. Further, temperature affects the reaction kinetics and transport properties such as resistivities, diffusivities and membrane solubilities--seemingly all related to the amount of water absorption in the membrane [29]. Thus, appropriate thermal and water management are critical for PEM fuel cell performance.

The temperature rise within a PEM fuel cell results from the heat generation due to the exothermic nature of the overall reaction, Joule heating and the phase change of water. For the results shown in Fig. 7, the contribution from the condensation of water vapor is small because the relative humidity of the reactant gas streams is set at 100%. In some working cells the gas streams are introduced into the cell at temperatures above the cell operating temperature in order to provide a larger quantitity of water vapor for membrane hydration. This technique will result in the condensation of excessive water vapor present, accompanied with heat release in the cell, thus, potentially increasing the temperature. Fig. 8a shows the temperature profile for the reactant gas humidity of 110% to simulate saturated, higher temperature feed streams. It is seen that the effect of water condensation in the cell is the most prominent at low current density of 0.1 A/cm^2 where the peak temperature is about twice of what is shown in Fig. 7. This is because at low current densities Joule heating and heat of reaction is small and the heat of condensation dominates. However, Joule heating increases significantly with the current density and becomes dominant at high current densities. As shown in Fig. 8a, the peak temperature decreases slightly at 1.1 A/cm^2 because of reduced membrane resistivity due to better hydration.

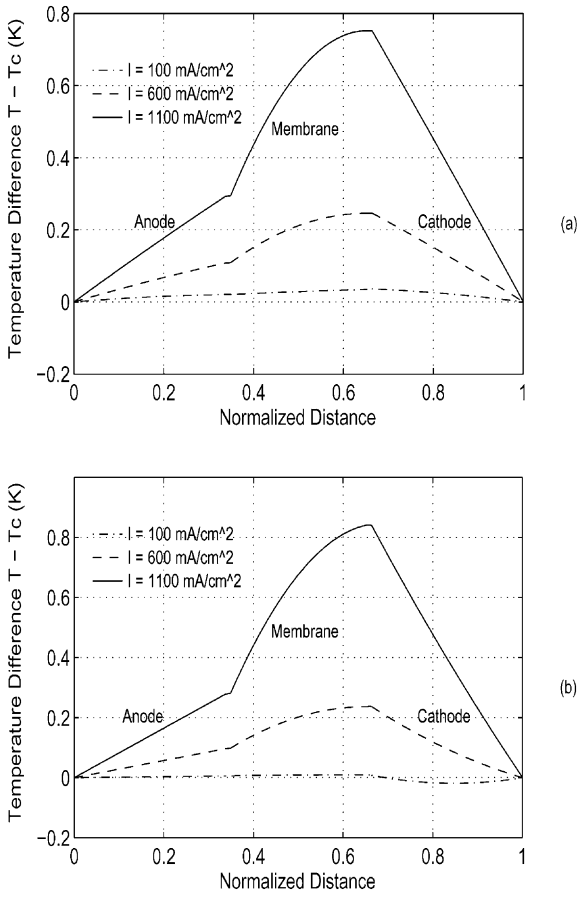

Fig. 8. Temperature profile over the entire cell for gas feed stream humidities of 110% (a); and oxidant stream humidity of 50% (b).

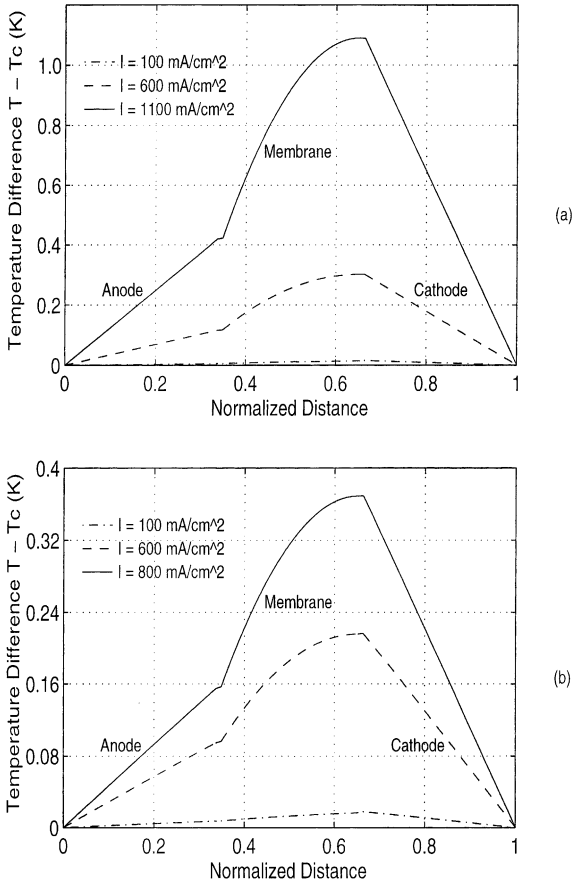

Fig. 9. Temperature profile over the entire cell for the cell operating temperature of $T_c = 333$ K (a); and 368 K (b).

Similarly, the effect of water vaporization in the cell can be simulated by the use of unsaturated reactant streams, as shown in Fig. 8b for the relative humidity of 50% in the cathode gas stream. The effect of liquid vaporization is clearly evident at 0.1 A/cm^2 driving the temperature down. This can be seen at higher current density of 0.6 and 1.1 A/cm^2 as well, as the slight depression in the temperature profile across the cathode electrode.

Fig. 9 shows the temperature distribution across the cell for the cell operating temperature of $T_c = 60°C$ and 95°C. It is seen that the peak temperatures within the cell for $T_c = 60°C$ (Fig. 9a) are larger than those shown in Fig. 7 obtained for $T_c = 80°C$, whereas the maximum temperatures at the high current density of 0.6 and 0.8 A/cm^2 given in Fig. 9b are less than the corresponding peaks in Fig. 7. It, therefore, suggests that the temperature distribution tends to be more uniform as cell operating temperature is increased. Although the predicted temperature difference through the cell is small (on the order of 1 K), the effects in a complete fuel cell stack could be significant where cooling plates are distributed periodically throughout the stack. Obviously, thermal conductivities of the cooling plates, flow channel plates (i.e. bipolar plates) and electrodes impact heat transfer through the cell. To simulate the effects of cooling and

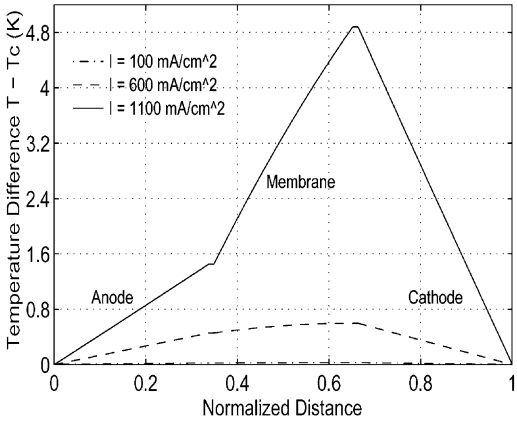

Fig. 10. Temperature profile over the entire cell for electrode thermal conductivity of 0.004 W/cm K and a cell temperature of 353 K.

bipolar plates which are typically at least one order of magnitude thicker than the electrodes, the electrode thermal conductivities are set to one-fourth of their base case values, and the resulting temperature profile is shown in Fig. 10. Clearly, the temperature within the cell is much higher with these reduced thermal conductivities, and the peak temperature difference becomes nearly 5 K at 1.1 A/cm^2. Therefore, as it is well known, the thermal and water management for a stack are much more demanding than for a single cell.

Fig. 11 shows the distribution of liquid water flux and relative humidity within the cathode electrode for the oxidant stream relative humidity of 50%. It is seen in Fig. 11b that the relative humidity increases from the oxidant gas flow channel of 50 to about 78% at the electrode/catalyst layer interface, and it increases only slightly with the current density. This increase of the relative humidity in the cathode is a direct result of liquid water vaporization. Fig. 11a shows that at high current density of 0.6 A/cm^2, the liquid water flux remains positive throughout the cathode, implying that liquid water from the cathode catalyst layer is used to satisfy the vaporization requirement. However, at the low current density of 0.1 and 0.2 A/cm^2, water flux is positive near the region close to the catalyst layer, while it becomes negative near the region next to the oxidant flow channel. Thus, it indicates that the liquid water from the catalyst layer is insufficient to meet the need of vaporization; and liquid water flowing in from the cathode flow channels (negative flux) is needed to maintain the steady-state operation assumed. With a stream inlet humidity of 50%, however, there will be no liquid water available from the flow channels. Therefore, dehydration of membrane will occur.

The results for 75% relative humidity in the anode gas stream are given in Fig. 12 . It is seen in Fig. 12a that the relative humidity in the anode electrode increases from the anode flow channels to the anode catalyst layer. This is due to the decreasing hydrogen concentration profile set up in the anode for hydrogen transport to the catalyst layer for electrochemical reactions there. Since the total pressure (hence, the total gas species concentration) is assumed to

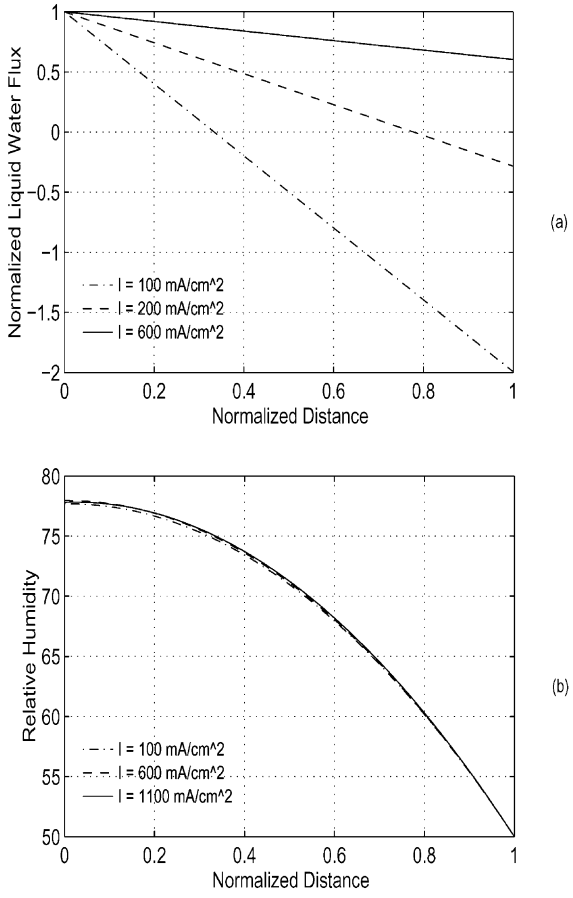

Fig. 11. Distribution of liquid water flux and relative humidity within the cathode electrode for the oxidant stream relative humidity of 50%. In (a), a positive flux indicates water would have to flow away from the catalyst layer towards the gas channel. A negative flux is in the opposite direction.

be constant in the anode, decreasing hydrogen concentration is reflected as the increase in the water vapor concentration, thus, the relative humidity increases. When the current density is increased from 0.1 to 0.6 A/cm^2, the relative humidity increases slightly as well. This phenomenon may be attributed to the fact that the increasing rate of hydrogen consumption with the higher current density sets up steeper hydrogen concentration profile in the anode, leading to the slight increase in the relative humidity. Temperature effect may also contribute to the phenomenon. Fig. 12b shows the net water flux per proton across the membrane for both 75 and 100% (base case condition) relative humidity in the anode gas stream. It is seen that at low current densities, the net water flux is negative, indicating that water is transported from the cathode to the anode due to back diffusion arising from the water concentration gradient. However, at high current densities, the net water flux becomes positive, signifying the dominant effect of electro-osmotic drag on water transport. The low humidity at the anode results in local drying of the membrane at the anode side, leading to increased membrane resistance to proton transport. As a result, Ohmic losses in

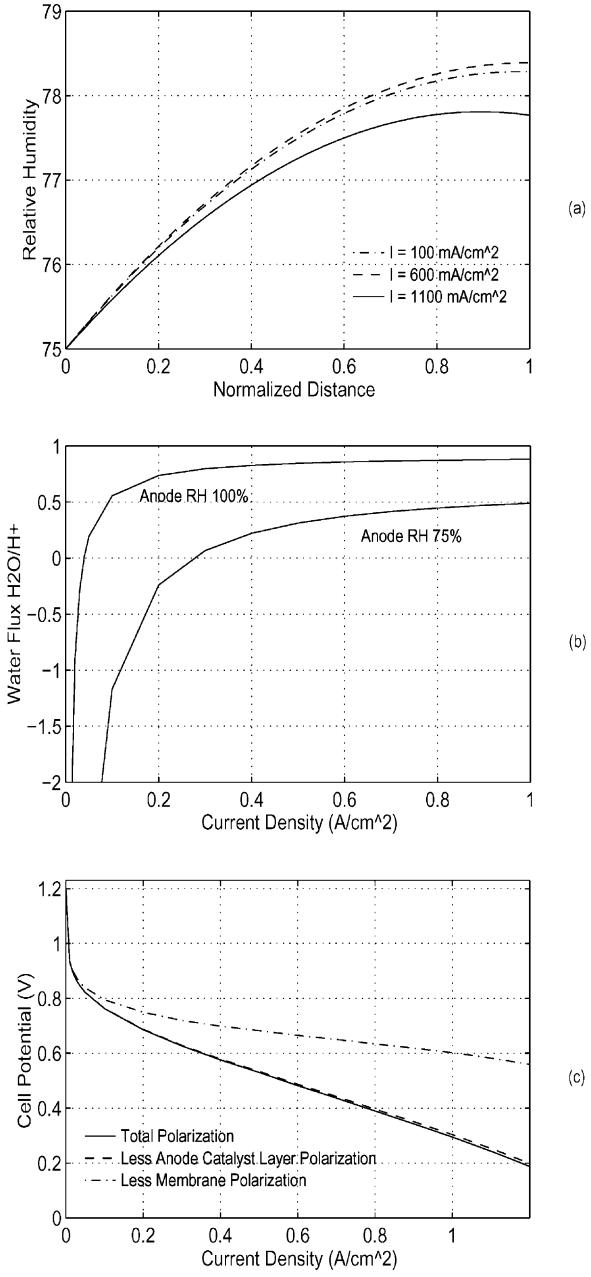

Fig. 12. Distribution of relative humidity within the anode electrode (a); net water flux across the membrane (b); and cell polarization curve (c) for 75% relative humidity in the anode gas stream.

the membrane becomes larger than for a fully humidified fuel stream, and the overall cell performance is greatly reduced. This is evident for the cell polarization curve shown in Fig. 12c and when it is compared with the corresponding results in Fig. 3 for the fully humidified base case condition.

For PEM fuel cells to become a viable alternative to internal combusiton engines in transportation applications in the near term, the hydrogen used will have to be derived from an energy carrier with high volumetric energy density, typically hydrocarbon fuels, through an onboard reformer. In the case of steam reforming of methanol, the resulting mole

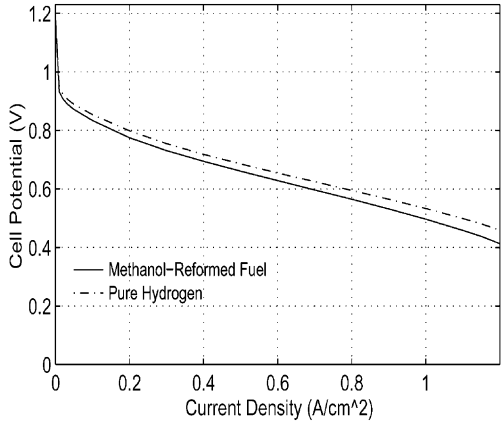

Fig. 13. Polarization for methanol-reformed fuel (mole fraction of CO_2 to H_2 is 0.25).

fraction of CO_2 relative to H_2 is approximately 0.25 in dry gas. The performance with such a methanol-reformed fuel stream is shown in Fig. 13. It is seen that the cell performance is reduced over the entire operating current density range when compared to the operation with pure hydrogen as fuel. This may, at first, be easily attributed to the decreased partial pressure of hydrogen in the reformed fuel stream. In reality, however, another loss mechanism is present as well. As shown earlier, a reduction of relative humidity in the anode causes increased losses due to decreased membrane hydration. A similar effect occurs with reformed fuel. This is because the presence of carbon dioxide reduces the diffusion coefficient of water vapor, limiting the amount of water diffusion from the anode gas stream to the anode catalyst layer, as shown in Fig. 14a for the pressure of 3 atm. It is clear that the reduction of relative humidity in the anode becomes significant at high current densities.

Similarly, a higher anode gas pressure decreases the diffusion coefficient of water vapor, because the diffusion coefficient is inversely proportional to the total pressure. Therefore, higher operating pressures will result in steeper gradient for the water vapor, as shown in Fig. 14b for the total pressure of 10 atm. A comparison with Fig. 14a shows a significant decrease in relative humidity at the anode catalyst layer interface when the pressure is increased from 3 to 10 atm. This effect continues to increase with pressure. Fig. 15 presents the cell performance with methanol-reformed fuel stream at the pressure of 15 atm, along with a breakdown of the cell potential losses. Clearly, Ohmic losses in the membrane are considerable and increase with current density, as expected. These results suggest that water management in the anode is as important as in the cathode for operations at high pressures and with reformed fuels.

Cell performance for methanol-reformed fuel at various pressures is shown in Fig. 16. It is interesting to note from Fig. 16a that the cell potential increases with pressure at low current densities; but decreases with pressure at high current

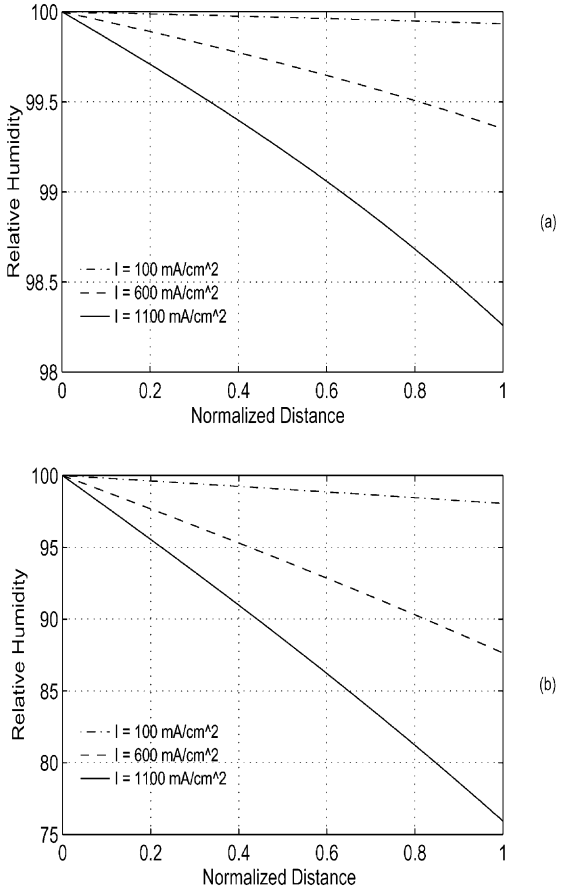

Fig. 14. Distribution of the relative humidity within the anode electrode with methanol-reformed fuel stream at 3 atm (a); and 10 atm (b).

densities primarily due to membrane dehydration near the anode side arising from the decreased water vapor flux in the anode. The corresponding power density in Fig. 16b indicates that the power density increases with pressure at low current densities, but the increment becomes smaller at higher pressures shown. The peak power density ocurrs at smaller current density as pressure is increased; and the maximum peak power occurs at the pressure of 10 atm.

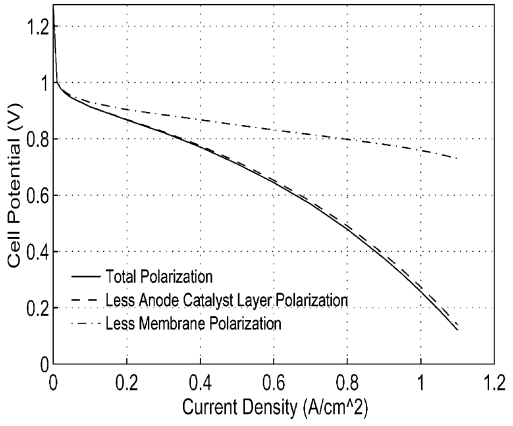

Fig. 15. Cell performance with methanol-reformed fuel stream at 15 atm.

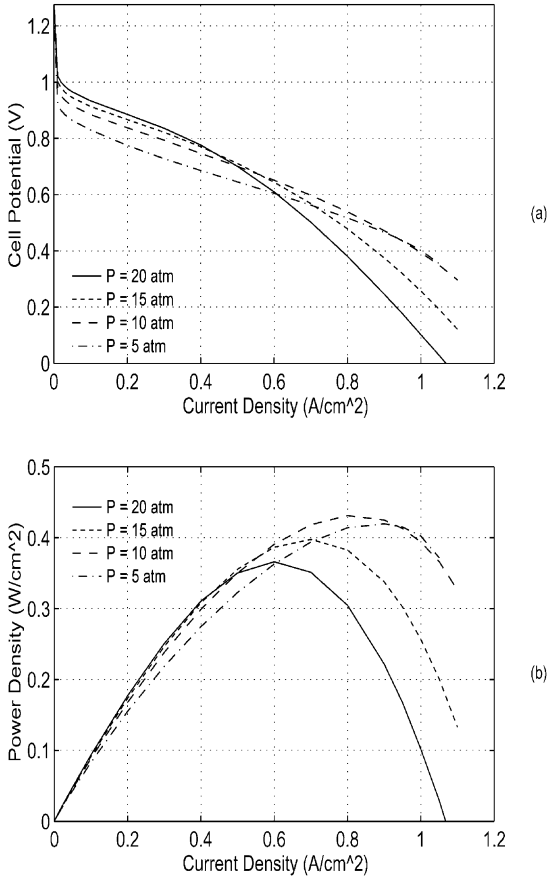

Fig. 16. Cell performance for methanol-reformed fuel at various pressures and $T_c = 353$ K. (a) polarization; (b) power density.

The power density for the pressure of $p = 20$ atm peaks at the current density of 0.6 A/cm^2 which corresponds to the cell potential of 0.6 V; this power density is about the same as that at $p = 5$ atm, and is smaller than that at $p = 10$ and 15 atm. Therefore, an optimal operating pressure exists even without considering other complexities associated with high pressure operations such as reactant compression, sealing and additional mechanical strength requirement. It should be noted that the results shown in Fig. 16 are obtained at the cell temperature of 80°C. Further calculations show that membrane dehydration at high pressures can be alleviated somewhat by increasing the cell operating temperature.

5. Conclusions

A one-dimensional non-isothermal model of a PEM fuel cell has been developed, and the effect of design and operating conditions on the cell performance, thermal response and water management have been investigated. It is found that water phase change in the electrodes affect the temperature profile, especially for unsaturated reactants and at low operating temperatures. The peak temperature rise in a single cell becomes larger at lower cell operating temperatures or for partially humidified reactant streams, and it could be significant for fuel cell stacks. It is observed that it may be possible to reduce the humidification of the cathode gas stream at high current densities if there is sufficient humidification in the anode to satisfy the water flux demands across the membrane. Cell performance suffers if suitable membrane hydration on the anode side is not maintained. Maintaining adequate membrane hydration at the anode side becomes significantly difficult for reformed fuels and for operations at high pressures, even when the anode gas stream is fully humidifed, because of reduced water vapor diffusion coefficient. As operating pressures are increased, water vapor concentration decreases in the anode electrode, resulting in decreased performance due to reduced membrane hydration. The results of the present study indicate that operating temperature and pressure can be optimized, based on cell performance, for given design and other operating conditions.

Acknowledgements

This work was carried out as a part of a large CRD project supported by the Natural Sciences and Engineering Research Council of Canada (NSERC), British Gas and Ballard Power Systems. Partial financial support was also provided by a research grant from the NSERC.

References

[1] D.M. Bernardi, Water balance calculations for solid polymer electrolyte fuel cells, J. Electrochem. Soc. 137 (11) (1990) 3344–3345.
[2] D.M. Bernardi, M.W. Verbrugge, Mathematical model of a gas diffusion elelctrode bonded to a polymer electrolyte, AIChE J. 37 (8) (1991) 1151–1163.
[3] D.M. Bernardi, M.W. Verbrugge, A mathematical model of the solid polymer electrolyte fuel cell, J. Electrochem. Soc. 139 (9) (1992) 2477–2491.
[4] J.-T. Wang, R.F. Savinell, Simulation studies on the fuel electrode of a H_2/O_2 polymer electrolyte fuel cell, Electrochim. Acta 37 (15) (1992) 2737–2745.
[5] T.A. Zawodzinski, T.E. Springer, S. Gottesfeld, Polymer electrolyte fuel cell model, J. Electrochem. Soc. 138 (8) (1991) 2334–2342.
[6] T.F. Fuller, J. Newman, Water and thermal management in solid polymer electrolyte fuel cells, J. Electrochem. Soc. 140 (5) (1993) 1218–1225.
[7] T.V. Nguyen, R.E. White, A water and heat management model for proton exchange membrane fuel cells, J. Electrochem. Soc. 140 (8) (1993) 2178–2186.
[8] M.S. Wilson, T.E. Springer, S. Gottesfeld, Modeling and experimental diagnostics in polymer electrolyte fuel cells, J. Electrochem. Soc. 140 (12) (1993) 3513–3526.
[9] W.R. Yong, O.A. Velev, S. Srinivasan, Mass-transport phenomena in proton exchange membrane fuel cells using O_2/He, O_2/Ar, and O_2/N_2 mixtures, J. Electrochem. Soc. 141 (8) (1994) 2084–2096.
[10] R.F. Mann, J.C. Amphlett, B.A. Peppley, On-board hydrogen purification for steam reformation/PEM fuel cell vehicle power plants, Int. J. Hydrogen Energy 21 (8) (1996) 673–678.

[11] J.C. Amphlett, R.M. Baumert, R.F. Mann, B.A. Peppley, P.R. Roberge, Performance modeling of the Ballard Mark IV fuel cell, J. Electrochem. Soc. 142 (1) (1995) 1–15.
[12] J. Kim, S.-M. Lee, S. Srinivasan, Modeling of proton exchange membrane fuel cell performance with an empirical equation, J. Electrochem. Soc. 142 (8) (1995) 2670–2674.
[13] S.A. Grot, K.R. Weisbrod, N.E. Vanderborgh, Through the electrode model of a proton exchange membrane fuel cell, Electrochem. Soc. Proc. 95 (23) (1995) 152–166.
[14] C. Marr, X. Li, Composition and performance modeling of catalyst layer in a proton exchange membrane fuel cell, J. Power Sources 77 (1999) 17–27.
[15] T.R. Ralph, G.A. Hards, J.E. Keating, S.A. Campbell, D.P. Wilkinson, M. Davis, J. St-Pierre, M.C. Johnson, Low cost electrodes for proton exchange membrane fuel cells, J. Electrochem. Soc. 144 (11) (1997) 3845–3857.
[16] C. Marr, X. Li, An engineering model of proton exchange membrane fuel cell performance, ARI 50 (1998) 190–200.
[17] J.J. Baschuk, X. Li, Modeling of polymer electrolyte membrane fuel cells with variable degrees of water flooding, J. Power Sources 86 (2000) 181–196.
[18] J.J. Baschuk, X. Li, Carbon monoxide poisoning of proton exchange membrane fuel cells. Int. J. Energy Res., 2000, in press.
[19] M. Wohr, K. Bolwin, W. Schnurnberger, M. Fischer, W. Neubrand, G. Eigenberger, Dynamic modeling and simulation of a polymer membrane fuel cell including mass transport limitation, Int. J. Hydrogen Energy 23 (3) (1998) 213–218.
[20] T.E. Springer, T.A. Zawodzinski, M.S. Wilson, S. Gottesfeld, Characterization of polymer electrolyte fuel cells using ac impedance spectroscopy, J. Electrochem. Soc. 143 (2) (1996) 587–599.
[21] A.M. Rowe, Mathematical modeling of proton exchange membrane fuel cells, Master's thesis, University of Victoria, Victoria, Canada, 1997.
[22] D. Fan, R.E. White, Modification of Newman's band (j) subroutine to multi-region systems containing interior boundary conditions: M-band, J. Electrochem. Soc. 138 (6) (1991) 1688–1691.
[23] C.R. Derouin, E.A. Ticianelli, S. Srinivasan, Localization of platinum in low catalyst loading electrodes to attain high power densities in SPE fuel cells, J. Electroanal. Chem. 251 (1988) 275–295.
[24] J.G. Beery, E.A. Ticianelli, S. Srinivasan, Dependence of performance of fuel cells with low platinum loading on morphologic characteristics of the electrodes, J. Appl. Electrochem. 21 (1991) 597–605.
[25] J. Fournier, G. Faubert, J.Y. Tilquin, R. Cote, D. Guay, J.P. Dodelet, High-performance, low Pt content catalysts for the electroreduction of oxygen in polymer electrolyte fuel cells, J. Electrochem. Soc. 144 (1) (1997) 145–154.
[26] M. Uchida, Y. Aoyama, N. Eda, A. Ohta, Investigation of microstructure in the catalyst layer and effects of both perfluorosulfonate ionomer and PTFE-loaded carbon on the catalyst layer of polymer electrolyte fuel cells, J. Electrochem. Soc. 142 (12) (1995) 4143–4149.
[27] A.K. Vijh, S. Ye, L.H. Dao, A new fuel cell electrocatalyst based on highly porous carbonized polyacrylonitrile foam with very low platinum loading, J. Electrochem. Soc. 143 (1) (1996) L7–L9.
[28] H.H. Voss, D.P. Wilkinson, K. Prater, Water management and stack design for polymer fuel cells, J. Power Sources 49 (1994) 117–127.
[29] S. Srinivasan, A. Parthasarathy, A.J. Appleby, Temperature dependence of the electrode kinetics of oxygen reduction at the Pt/Nafion interface — a microelectrode investigation, J. Electrochem. Soc. 139 (9) (1992) 2530–2537.
[30] T.A. Zawodzinski, C. Derouin, S. Radzinski, R.J. Sherman, V.T. Smith, T.A. Springer, S. Gottesfeld, Water uptake by and transport through Nafion 117 membranes, J. Electrochem. Soc. 140 (4) (1992) 1041–1047.
[31] T.A. Zawodzinski Jr., T.A. Springer, J. Davey, R. Jestel, C. Lopez, J. Valero, S. Gottesfeld, A comparitive study of water uptake and transport through ionomeric fuel cell membranes, J. Electrochem. Soc. 140 (7) (1993) 1981–1985.
[32] K. Broka, P. Ekdunge, Oxygen and hydrogen permeation properties and water uptake of Nafion 117 membrane and recast film for PEM fuel cell, J. Appl. Electrochem. 27 (1997) 117–123.
[33] J.M. Prausnitz, R.C. Reid, T.K. Sherwood, The Properties of Gases and Liquids, 3rd Edition, McGraw-Hill, New York, 1977.